Inorganic Chemistry

Article

pubs.acs.org/IC

Phase-Selective Synthesis of Cu_2ZnSnS_4 Nanocrystals using Different Sulfur Precursors

Zhenggang Li,[†,‡] Alvic Lim Kar Lui,[†] Kwan Hang Lam,[†] Lifei Xi,[§] and Yeng Ming Lam*[,†,‡,∥]

[†]School of Materials Science and Engineering, Nanyang Technological University, Blk N4.1, Nanyang Avenue, Singapore 639798
[‡]Energy Research Institute@NTU (ERI@N), Research Technoplaza Level 5, Nanyang Drive, Singapore 637553
[§]Semiconductor Nanoelectronics (PGI-9), Forschungszentrum Jülich GmbH, D-52425 Jülich, Germany
[∥]Institute of Materials for Electronic Engineering II, RWTH-Aachen, Sommerfeldstr. 24, D-52074 Aachen, Germany

S *Supporting Information*

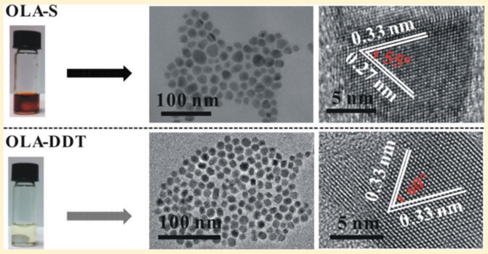

ABSTRACT: Cu_2ZnSnS_4 (CZTS) holds great promises as an absorber material for sustainable and low cost thin film solar cells. Kesterite and wurtzite are two common phases of CZTS. Until now, the synthesis and the growth of both phases are not clearly understood. In this work, kesterite CZTS nanoparticles, wurtzite CZTS nanoparticles as well as CZTS particles with a mixture of both structures were prepared by using elemental sulfur, 1-dodecanethiol, and thioacetamide, respectively. Time dependent studies were conducted and the reaction rate of sulfur source was found to be the key factor in determining the phase formation. Elemental sulfur reacts with oleylamine to produce highly reactive small molecule H_2S, which leads to the formation of kesterite phase. The reaction pathways of the long alkane chain 1-dodecanethiol yield the formation of wurtzite phase via a binary phase. Thioacetamide yields a mixture of kesterite and wurtzite phase in the final product. The optical and electrical properties of kesterite and wurtzite CZTS were also evaluated.

1. INTRODUCTION

Quaternary chalcogenide Cu_2ZnSnS_4 (CZTS), with a direct band gap of around 1.5 eV and an absorption coefficient of the order of 10^4 cm^{-1}, is a particularly suitable material for thin film solar cells. Since CZTS consists of only nontoxic and earth-abundant elements, it offers the added advantages of being low-cost and the technology being environmentally sustainable.[1−3] High conversion efficiency of 8.4% were achieved for solar cells based on system containing purely S and 11.1% based on system containing both S and Se.[4,5] In the past decade, various deposition methods have been developed to prepare CZTS thin films including thermal evaporation, sputtering, electro-deposition, spray pyrolysis, nanoparticles ink approach and hybrid solution-particles approach.[6−12] The nanoparticles ink approach has drawn a wide interest due to its potential application in low cost manufacturing processes associated with solution-based methods.[13−15] The CZTS nanoparticles is dispersed in solvents to form the "ink" which can then be deposited onto substrates to form CZTS thin film using techniques such as spin-coating, spraying, drop-casting and doctor blading. Guo and co-workers synthesized CZTS nanocrystals via hot injection method and these nanoparticles was then used for the fabrication of solar cells with efficiency of up to 7.2%.[16]

The most common phase structure obtained for CZTS is the zinc blende derived structures, of which kesterite and stannite are the two low-energy polytypes.[17] These two polytypes have different cation orderings: the kesterite lattice has alternating cation and anion layers in the order of CuZn/SS/CuSn/SS along crystallographic *c*-direction, while for the stannite lattice, this ordering changes to CuCu/SS/ZnSn/SS.[10] Both theoretical calculation and experimental work have shown that the kesterite structure is the lower energy form and is thus more thermodynamically stable than the stannite structures.[17,18] Recently, wurtzite-type CZTS has been reported by several different research groups.[19−22] Lu and co-workers synthesized wurtzite CZTS nanostructures, which adopted a hexagonal unit cell.[19] Other wurtzite-related phases or more accurately wurtzite−kesterite and wurtzite−stannite phases were also reported.[23,24] Despite the excellent progress in the synthesis and preparation of different polytypes of CZTS accompanied by some propositions on the effect of 1-dodecanethiol in the synthesis of hexagonal phase CZTS, there is little conclusive evidence on the possible factors that could influence phase formation. In addition, the formation mechanisms of the above CZTS polytypes were also not clearly understood.

Figure 1 shows the unit cell structures of CZTS kesterite and wurtzite. The cations in the kesterite structure (Figure 1a) sit in the tetrahedral sites surrounding the sulfur anions. In the Cu/Zn layer, due to the small energy differences, the positions of Cu and Zn are interchangeable, and the Cu and Zn ions can be considered as randomly distributed in this layer. In the wurtzite structure (Figure 1b), sulfur anions are located in the hexagonal

Received: April 29, 2014
Published: September 29, 2014

dx.doi.org/10.1021/ic500956n | *Inorg. Chem.* 2014, 53, 10874−10880

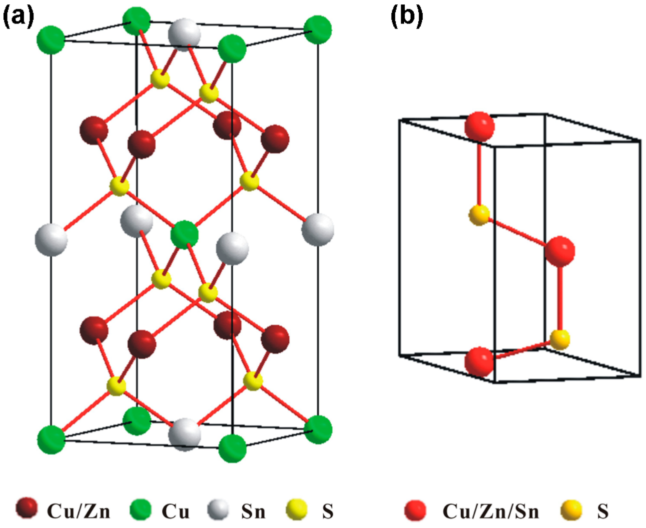

Figure 1. Unit cell structure of CZTS (a) kesterite (in the Cu/Zn layer, the Cu and Zn ions have equal occupancy of 0.5) and (b) wurtzite (the red ion represents Cu, Zn, or Sn ions with the 0.5 occupancy of Cu ion, 0.25 occupancy of Zn ion, and 0.25 occupancy of Sn ions).

close packed positions; Cu(I), Zn(II), and Sn(IV) cations randomly occupy half of the interstices of the sulfur anions. The ratio of Cu, Zn, and Sn ions is maintained at 2:1:1.

Differences in phase structure have an effect on material property. For example, calculations based on density functional theory showed that kesterite structure is thermodynamically more stable than stannite polytypes of CZTS.[17,18] In the past, stoichiometry changes were commonly used to change the band gap in CZTS, but more recently, it has been shown that structural variations can also alter the bandgap.[25] On top of all these phase-dependent properties, there is another important advantage of being able to selectively control the phase formation, and that is the transformation of metastable phase-required lower energy. This advantage is shown recently in the transformation of metastable wurtzite phase at relatively low temperature that drives grain growth.[26] In view of all these advantages, the understanding of what promotes the formation of kesterite and wurtzite phases are urgently needed. On top of this, the impact of structural differences on the optical properties will also need to be better understood.

In this work, we report the controlled synthesis of CZTS nanoparticles with different crystallographic phases by simply tuning the sulfur sources. Essentially, elemental sulfur (S), 1-dodecanethiol (DDT), and thioacetamide (TAA) were dissolved in oleylamine (OLA) and used as the sulfur precursors. Using these three precursors, kesterite, wurtzite, mixed kesterite and wurtzite type CZTS were formed. To understand why this happened, time-dependent studies were performed to investigate the formation mechanism of kesterite and wurtzite CZTS. It was found that the reaction rate of S source determines the phase formation of CZTS: the highly reactive OLA−S leads to an immediate precipitation of kesterite CZTS; the less reactive OLA−DDT results in the formation of Cu_7S_4 at the early stage and then gradually developed into wurtzite CZTS; and the moderately reactive OLA−TAA yields a mixture of kesterite and wurtzite CZTS in the final product. In addition, the optical and electrical properties of kesterite and wurtzite phases were evaluated and compared based on UV−vis−NIR absorption measurements and cyclic voltammetry techniques.

2. EXPERIMENTAL DETAILS

Materials. Copper(II) acetate ($Cu(OAc)_2$, Aldrich, 98%), zinc chloride anhydrous ($ZnCl_2$, Sigma-Aldrich, 99.99%), tin(IV) chloride pentahydrate ($SnCl_4.5H_2O$, Sigma-Aldrich, 98%), elemental sulfur (S, Aldrich), oleylamine (OLA, Aldrich, 70%), 1-dodecanethiol (DDT, Aldrich, 98%), thioacetamide (TAA, Sigma-Aldrich, 98%), toluene (Aik Moh Paints & Chemicals), and ethanol (Aik Moh Paints & Chemicals, 95%) were purchased and used as received.

Synthesis. CZTS nanocrystals were synthesized using hot injection method. In a typical synthesis, 0.5 mmol $Cu(OAc)_2$, 0.25 mmol $ZnCl_2$, 0.25 mmol $SnCl_4 \cdot 5H_2O$, and 5 mL of OLA were mixed in a 50 mL three-neck flask. The mixture was then pumped under vacuum conditions for 30 min to remove moisture or O_2. Subsequently, the mixture was purged with N_2 gas and heated to 150 °C. The temperature was maintained at 150 °C for 30 min to form stable Cu-, Zn-, and Sn-OLA coordinating complex or metal precursors. After that, the mixture was heated rapidly to 235 °C, where the injection of sulfur precursors took place. The sulfur precursor was prepared by dissolving/mixing 1 mmol sulfur source with 1 mL of OLA at room temperature. Three different types of sulfur source were used, and they are elemental sulfur (S), 1-dodecanethiol (DDT) as well as thioacetamide (TAA). The reaction temperature was maintained at 235 °C for 1 h before cooling to room temperature. The as-prepared CZTS nanoparticles were washed several times using toluene and ethanol. From here onward, the nanoparticle products synthesized from elemental S, DDT, and TAA will be denoted as sample S, sample DDT, and sample TAA, respectively.

Characterization. The grazing incidence X-ray diffraction (GIXRD) patterns of the thin films were collected using Bruker D8 Advance equipped with Cu Kα radiation ($\lambda = 1.54$ Å). The diffraction patterns were collected at a fixed incident angle of 1° and were collected from 20° to 70° in steps of 0.05°. The atomic ratio of Cu, Zn, Sn, and S was measured with an accelerating voltage of 20 keV using an Oxford X-MAX energy dispersive X-ray spectroscopy (EDS) detector, which is equipped on a JEOL JSM 7600F FESEM. The Raman analysis was performed using a WITec confocal Raman spectroscope with a 532 nm laser, which provided an extra evidence for the formation of CZTS compound in addition to XRD. The transmission electron microscopy (TEM) analysis was performed using a JEOL 2100F with a field emission source and at an accelerating voltage of 200 kV. The UV−vis absorption spectra were obtained using a Shimadzu UV−vis−NIR PerkinElmer Lambda 900 spectrophotometer. Cyclic voltammetry (CV) measurements were performed using an Autolab PG302N electrochemical workstation. Carbon and gold electrodes were used as working and counter electrodes, respectively, with Ag/AgCl electrode as reference electrode. CZTS samples were coated onto working electrode by drop casting CZTS nanoparticles suspension in chloroform.

3. RESULTS AND DISCUSSIONS

CZTS nanoparticles were synthesized using three different sulfur precursors, namely, S, DDT, and TAA. From here onward, the samples synthesized using the different precursors will be referred to according to the sulfur precursors used. Figure 2 shows the XRD patterns of the as-synthesized nanoparticles. It can be seen that sample S matched very well with kesterite CZTS (JCPDS No. 26−0575). The XRD pattern shows three major peaks at 28.5°, 47.6° and 56.3°, corresponding to (112), (220), and (312) lattice planes, respectively. The results are in good agreement with the previously reported data for kesterite CZTS.[13,14] For sample DDT, a totally different XRD pattern is observed, and this can be matched to the simulated diffraction pattern of wurtzite CZTS structure. The major XRD peaks at 26.9°, 28.3°, 30.2°,

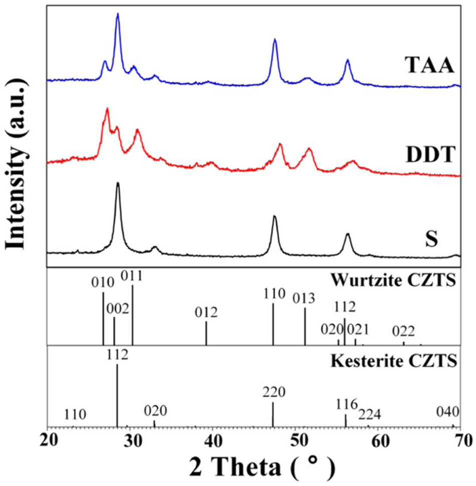

Figure 2. XRD patterns of as-synthesized samples using elemental S, DDT, and TAA as the sulfur source. The XRD pattern for kesterite CZTS (JCPDS No. 26−0575) and simulated XRD pattern for wurtzite CZTS are also presented and indexed for comparison.

47.6°, 51.0°, and 56.2° can be observed for sample DDT, which indicates that this sample is essentially wurtzite CZTS. As for sample TAA, the XRD pattern shows a mixture of kesterite and wurtzite phases. Using Rietveld refinement, it is found that this sample consists of 50.3 wt % kesterite and 49.7 wt % wurtzite (refer to Supporting Information, Figure S1). The Cu/Zn/Sn/S ratios were determined by SEM EDS for sample S (2.07:0.91:0.88:4.00), sample DDT (2.41:0.74:1.10:4.00), and sample TAA (2.18:0.97:1.14:4.00), respectively.

Besides structural analysis using XRD, Raman spectroscopy was also performed to confirm the formation of CZTS phases. The Raman shifts of kesterite CZTS were reported to be 288 cm^{-1}, 338 cm^{-1}, and 368 cm^{-1}, where the 338 cm^{-1} peak represents the Raman A mode of CZTS.[27,28] A slight shift in Raman peak positions can often be observed which may be due to the differences in preparation methods and compositions.[29] The wurtzite CZTS have similar Raman A mode shifts to those of the kesterite structure. Singh et al. reported a strong Raman peak at 333 cm^{-1} for wurtzite CZTS nanorods.[20] As shown in Figure 3, the Raman A mode sample S exhibits a strong single peak at 336 cm^{-1}, which is indicative of kesterite CZTS. The two shoulder peaks at ∼288 and 368 cm^{-1} could also be noticed, which also match well to kesterite CZTS. For sample DDT, the Raman A mode peaks at 334 cm^{-1} also agrees well with CZTS. The shoulder peak at 288 cm^{-1} is visible, while the one at 368 cm^{-1} is less obvious. As for sample TAA, the major peaks at 336 cm^{-1} and two shoulder peaks at 288 and 368 cm^{-1} could also be observed. During this synthesis of quaternary CZTS, the binary and ternary sulfide phases are usually formed as impurity phases.[30,31] Among them, the Cu_2S (JCPDS No. 4−15−2234), ZnS (JCPDS No. 5−0566), and Cu_2SnS_3 (JCPDS No. 1−089−4714) share similar crystal structure as well as XRD patterns with CZTS. Hence, Raman analysis is necessary in addition to XRD to confirm the formation of CZTS phase. From our Raman results, no noticeable peaks corresponding to Cu_2S (475 cm^{-1}), ZnS (278 and 351 cm^{-1}), or Cu_2SnS_3 (298 and 356 cm^{-1}) can be observed.[32−34] Therefore, the Raman results confirm the formation of quaternary CZTS phases rather than binary or ternary phases for all the three samples.

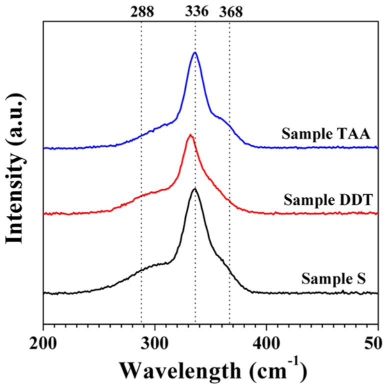

Figure 3. Raman shifts of sample S, sample DDT, and sample TAA. The peak positions of 288, 336, and 368 cm^{-1} are marked by dotted lines.

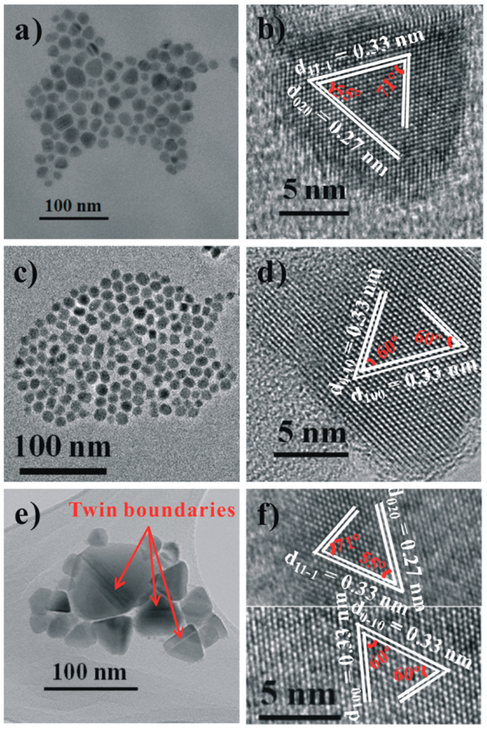

Figure 4. TEM images of (a) sample S, (c) sample DDT, and (e) sample TAA and the HRTEM images of (b) sample S, (d) sample DDT, and (f) sample TAA. The lattice spacings for the various particles are shown in the HRTEM images.

TEM images of CZTS nanoparticles synthesized using elemental S as the sulfur source are shown in Figure 4a,b. These CZTS nanoparticles have irregular shape and possess an average size of 19.8 ± 6.5 nm. From the HRTEM image (Figure 4b), the lattice spacings were found to be 0.33 and 0.27 nm, which correspond to the *d*-spacing of $(11\bar{1})$ planes and (020) planes, respectively, for kesterite CZTS.[14] To distinguish the two similar polymorphs—kesterite and zinc blende—select area electron diffraction (SAED) patterns were also collected (refer to Supporting Information, Figure S2). The rings associated with (211) and (105) planes, unique to the kesterite structure, were observed and hence confirm that the phase formed is mostly kesterite. The TEM images of CZTS nanoparticles synthesized using DDT are shown in Figure 4c,d. The nanoparticles are nearly spherical in shape, with an average diameter of 12.9 ± 1.2 nm. The HRTEM image (Figure 4d) shows that there are two lattice spacings of 0.33 nm each, which is consistent with the *d*-spacings of $(1\bar{1}0)$ planes and (100) planes, respectively, for wurtzite-type CZTS.[19] Figure 4e,f shows the TEM images of CZTS nanoparticles synthesized using TAA. Interestingly, the twin boundary defects are clearly observed in these nanoparticles. Looking at the HRTEM image (Figure 4f), both the kesterite and wurtzite CZTS can be observed in different nanoparticles. Fan and co-workers have also reported the formation of nanoparticles with both kesterite and wurtzite phases for CZTSSe nanoparticles, and in that case, both phases coexist in a single particle; this phase formation is controlled by the reaction temperature.[35] It is also worth noting that the kesterite CZTS nanoparticles (Figure 4a) generally have a polydisperse size distribution.[13,14] This is again most probably due to the fast reaction rate when elemental S is used as the precursor, and this resulted in a growth process that is not diffusion limited, and in both nucleation and growth occurred simultaneously. The detailed mechanism involving sulfur as the precursor will be discussed later. On the other hand, the wurtzite CZTS nanoparticles (Figure 4c) have a size distribution that is more mono-dispersed, suggesting a slow reaction dynamics.

To control the development of kesterite and wurtzite phases, it is important to understand the growth mechanism that resulted in the two phases. Time-dependent studies were carried out to study the phase evolution for both kesterite (sample S) and wurtzite samples (sample DDT). Samples were extracted at various intervals: 10 min, 30 min, 1 h, and 2 h. From the XRD patterns of sample S in Figure 5, it can be observed that highly crystalline kesterite CZTS phase exists in this sample. There are weak but noticeable non-CZTS peaks, which could be attributed to binary or ternary impurity phases that are commonly observed in films synthesized via solution routes.[30] Even as early as 10 min after the injection, the diffraction peaks observed are at 28.5°, 47.6°, and 56.3°, and they are all characteristic of kesterite phase. This indicates that the reaction process is very fast. All the other samples extracted after 30 min, 60 min, and 2 h also matched well with crystalline kesterite CZTS phase. These findings suggest that the formation of kesterite CZTS occurred rapidly, and since this reaction is fast, there is very little morphological control as seen in the TEM images in Figure 4.

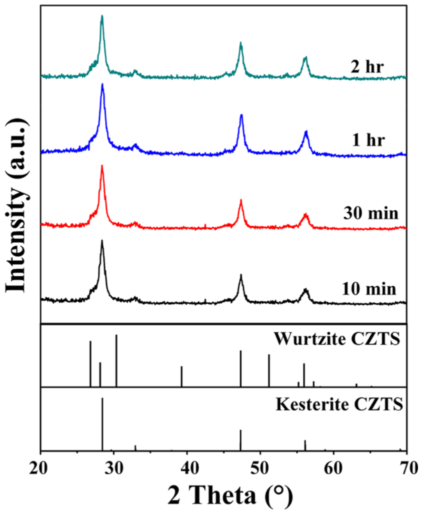

Figure 5. XRD patterns of sample S extracted at 10 min, 30 min, 1 h, and 2 h. The XRD patterns for kesterite CZTS and wurtzite CZTS are also presented for comparison.

With different S precursors, there is a possibility to moderate the growth process. Instead of using elemental S, as shown earlier, DDT can also be used as the S source to produce CZTS nanoparticles. In the case of DDT, there is a long alkyl chain that can moderate the phase evolution process. The XRD patterns for sample DDT extracted at the time intervals of 10 min, 30 min, 1 h, and 2 h are shown in Figure 6. After the first 10 min, only Cu_7S_4 binary sulfide phase is formed, indicating that DDT first preferentially reacts with the Cu species. After 30 min, in addition to the dominant Cu_7S_4 phase, XRD peaks at 26.9°, 30.2°, and 51.0° are observed, which suggests the formation of wurtzite CZTS phases. At 60 min, the crystallinity of the sample improved substantially, and all the major XRD peaks associated with wurtzite CZTS can be observed. The minor peaks at 34.2° and 37.8° corresponding to Cu_7S_4 could still be observed. When the reaction time further increases to 2 h, the XRD pattern appears very similar to that observed for 60 min where both wurtzite CZTS and Cu_7S_4 coexisted. In contrast to the synthesis of kesterite CZTS nanoparticles using S as the precursor, the nanoparticles synthesized using DDT went through a slower phase evolution process via a binary phase for wurtzite CZTS nanoparticles. Binary Cu_7S_4 phase was formed at the early stage of the reaction. From the XRD data, it can be seen that over time there is an increase in the wurtzite CZTS phase and a decrease in the Cu_7S_4 phase.The formation of intermediate Cu_7S_4 phase and its gradual development into wurtzite phase indicate that DDT will result in a slower reaction rate. The size of the resultant nanoparticles is more uniform. At this moment the exact nature of the transformation between the phases in these nanoparticles is unclear and is the subject of ongoing research.

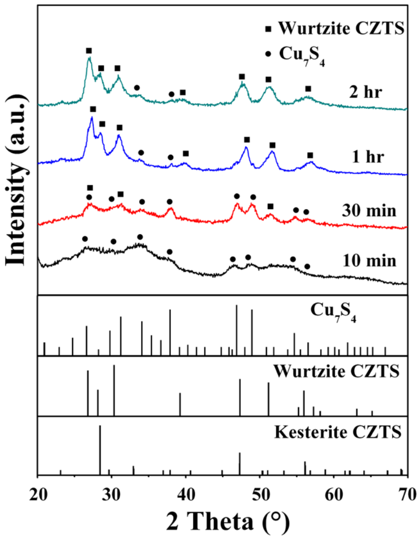

Figure 6. XRD patterns of sample DDT extracted at 10 min, 30 min, 1 h, and 2 h. The XRD patterns for kesterite CZTS, wurtzite CZTS, and Cu_7S_4 (JCPDS No. 23−0958) are also presented for comparison.

The phase development in CZTS nanoparticles is strongly related to the reactivity of sulfur precursors. Highly reactive elemental S yields fast formation of kesterite CZTS phase, while DDT results in a slow and gradual formation of wurtzite CZTS phase starting with the formation of binary Cu_7S_4

(JCPDS No. 23−0958). In an earlier work, it was found that sulfur and the amine group could react to form alkyl ammonium polysulfides at room temperature.[36] At elevated temperature, these polysulfide ions can easily react with excess amine to release H_2S.[37] In this reaction, OLA−S mixture is injected into metal complexes solution kept at above 200 °C, thus subjecting the OLA−S mixture to a high temperature, and this resulted in the formation of H_2S according to previous works.[36,37] After injection of OLA−S mixture, the color of solution mixture turned dark immediately. The H_2S produced by OLA−S mixture reacts rapidly with Cu-, Zn-, Sn-OLA complex, which leads to fast formation of kesterite CZTS nanoparticles. Considering the enthalpy of formation for the Cu-binary compound ($\Delta H_{\text{reaction}} = -79.5$ kJ/mol) compared to quaternary CZTS ($\Delta H_{\text{reaction}} = -525.1$ kJ/mol) calculated based on their elemental standard states, the formation of CZTS is indeed more favorable.[38,39] As the reaction between H_2S and the metal ions is very rapid, it is difficult to separate the nucleation and growth processes, which resulted in a wide size distribution.

The reaction with DDT molecule occurs at a slower rate. DDT molecule contains a 12 carbon chain and a thiol headgroup. The thiol group in DDT provides S for the formation of CZTS nanoparticles in this reaction. S is covalently bonded to one C and one H atom, making this a rather stable molecule compared to H_2S. After the injection of OLA−DDT mixture, the reaction mixture turned gradually from yellow to black in ∼10 min. This reaction undergoes a thiolate formation stage that involves the metal ions and the DDT. Cu ions can form stable complexes with thiol, and this can then be followed by the cleavage of C−S bonds that will then result in the formation of Cu-based binary sulfides. In this case, binary compound is very likely to be formed first followed by any of the other compounds. As shown in the diffraction patterns in Figure 6, the Cu_7S_4 phase was first formed in this reaction. Subsequently, Zn species, Sn species, and the remaining DDT reacted with Cu_7S_4 seed, which gradually evolved into the wurtzite CZTS phase. These results are in good agreement with previous the reports on wurtzite CZTS using DDT as sulfur source.[24] With the slower reaction rate of DDT, the growth process is controlled by the bond-breaking process to release S, and therefore a nearly monodispersed size distribution was obtained.

As for the case of TAA, it was reported that TAA could react with OLA to produce H_2S and long-chain N-substituted thioamides.[40] The chemical reactions between TAA and OLA are shown in Scheme 1, and this is adapted from the work of Petrov and co-workers.[40] As shown in the reaction scheme, reactions 1 and 3 produce H_2S, while reaction 2 forms N-substituted thioamides. The highly reactive H_2S leads to the production of kesterite phases, while the less reactive long-chain thioamides yield the formation of wurtzite phase. Therefore, a mixture of kesterite phase and wurtzite phase was obtained. Our findings agree well with a previous report, which suggests a phase selectivity for CZTS based on the reactivity of Zn and S precursors.[22]

Scheme 1. Reaction between TAA and OLA

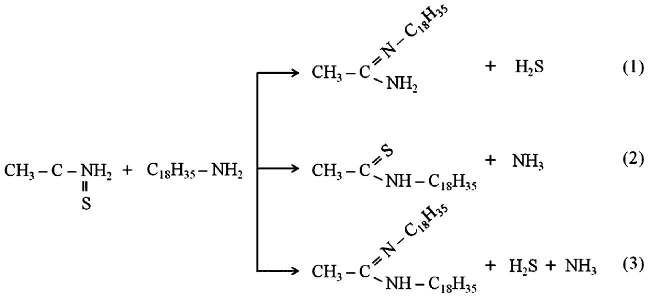

The optical properties of the as-prepared kesterite and wurtzite CZTS nanoparticles were investigated using UV−vis−NIR spectroscopy. Figure 7 shows the $(\alpha h\nu)^2$ versus $h\nu$ plots, which are used to calculate the optical band gap, where α is the absorption coefficient, h is Planck's constant, and ν is the frequency of light. The optical band gap can be derived by extrapolation of the linear region in each curve. The optical band gaps for kesterite and wurtzite CZTS are estimated to be 1.52 and 1.41 eV, respectively. The optical band gap for kesterite and wurtzite CZTS estimated based on UV−vis−NIR measurements agree well with previously reported band gap range for CZTS.[41]

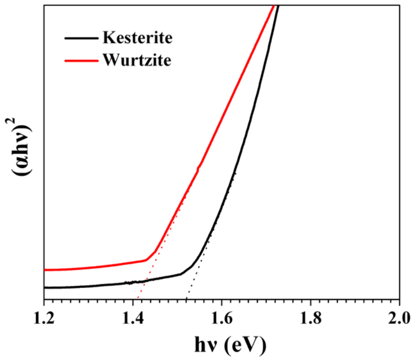

Figure 7. $(\alpha h\nu)^2$ vs $h\nu$ plot for as-prepared CZTS kesterite (sample S) and wurtzite (sample DDT) samples.

To investigate the conduction band (CB) and valence band (VB) levels of kesterite and wurtzite CZTS samples, CV analysis was performed on sample S and sample DDT. Ferrocene was used as the reference material for all CV measurements. The oxidation potential onset of ferrocene as marked by the vertical dotted line (Figure 8a) is estimated to be 0.3 V. Using ferrocene as the reference material, the CB and VB energy levels of the inorganic semiconductors can be calculated using the following equation:[42]

$$E_{\text{CB/VB}} = [(E_{\text{red/ox}} - E_{\text{ferrocene}}) + 4.7]\text{eV}$$

where $E_{\text{ferrocene}} = 0.3$ V.

In an earlier work, Huang and co-workers determined the CZTS kesterite VB of 5.19 eV and CB of 3.79 eV using Mott−Schottky plot.[43] Using ultraviolet photoelectron spectroscopy (UPS), Haight and co-workers estimated the two values to be 5.40 and 3.95 eV.[44] Figure 8b presents the CV results of sample S and sample DDT. On the basis of the results from Figure 8b, the reduction potential (E_{red}), oxidation potential (E_{ox}), CB energy level (E_{CB}), VB energy level (E_{VB}), and the electrical band gap (E_g) for both kesterite and wurtzite CZTS are calculated and presented in Table 1. As shown in Table 1, the VB and CB energy levels are −5.40 and −3.85 eV (sample S) and −5.43 and −3.91 eV (sample DDT). The VB and CB energy levels of CZTS kesterite (sample S) are similar to reported values.[44]

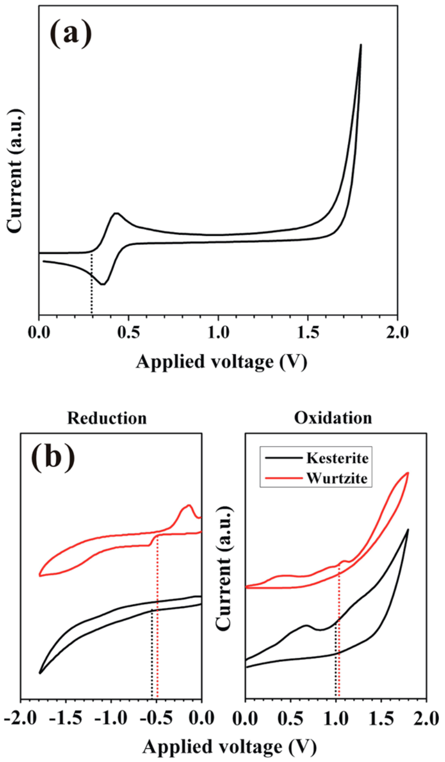

Figure 8. (a) The cyclic voltammograms of the oxidation potential of ferrocene as the internal standard to calibrate the measurements, and (b) cyclic voltammetry of CZTS nanoparticles samples prepared with elemental S (kesterite CZTS) and DDT (wurtzite CZTS) as the sulfur source.

Table 1. A Comparison of Conduction Band (CB) Energy Level, Valence Band (VB) Energy Level, As Well As the Electrochemical Band Gap of Kesterite CZTS and Wurtzite CZTS

CZTS samples	E_{red} (V)	E_{ox} (V)	E_{CB} (eV)	E_{VB} (eV)	E_g (eV)
kesterite	−0.55	1.00	−3.85	−5.40	1.55
wurtzite	−0.49	1.03	−3.91	−5.43	1.52

The electrochemical band gaps are determined by the difference between the VB and CB energy levels to be 1.55 and 1.52 eV for kesterite and wurtzite CZTS, respectively. Both values matched well with the reported band gap range of 1.4−1.6 eV for CZTS.[41] The slight discrepancies between electrical band gap and optical band gap could possibly arise from the interfacial energy barrier between CZTS samples with the electrode. Therefore, higher band gap values for CV measurements than optical measurements are expected.

4. CONCLUSION

In conclusion, we have successfully synthesized kesterite, wurtzite, and mixed kesterite−wurtzite CZTS nanoparticles using elemental S, DDT, and TAA as the sulfur source, respectively. It was found that the reactivity of the sulfur precursor plays a key role in determining the phase formation of CZTS nanoparticles. The elemental S could react with oleylamine to produce highly reactive small molecule H_2S, which then reacts with Cu, Zn, and Sn species to form kesterite CZTS nanoparticles. As for the case of DDT, the covalently bonded S is very stable and hence difficult to be broken down to release the S atom for the reaction, resulting in a slow reaction rate, and wurtzite phase is formed. TAA reacts with OLA to produce highly reactive H_2S and less reactive long-chain N-substituted thioamides, and therefore yields the formation of mixed kesterite and wurtzite phases. The optical band gap was estimated to be 1.52 and 1.41 eV for kesterite and wurtzite CZTS, respectively, based on UV−vis−NIR measurements. The VB and CB energy levels are determined using CV measurements to be −5.40 and −3.85 eV (kesterite CZTS) and −5.43 and −3.91 eV (wurtzite CZTS). The electrochemical band gaps were found to be 1.55 and 1.52 eV.

■ ASSOCIATED CONTENT

Ⓢ Supporting Information

TOPAS Rietveld refinement of CZTS samples prepared with TAA, compositional analysis of CZTS samples, electron diffraction patterns, enthalpy calculations. This material is available free of charge via the Internet at http://pubs.acs.org.

■ AUTHOR INFORMATION

Corresponding Author

*E-mail: ymlam@ntu.edu.sg.

Notes

The authors declare no competing financial interest.

■ REFERENCES

(1) Katagiri, H. *Thin Solid Films* **2005**, *480*, 426−432.
(2) Katagiri, H.; Jimbo, K.; Maw, W. S.; Oishi, K.; Yamazaki, M.; Araki, H.; Takeuchi, A. *Thin Solid Films* **2009**, *517*, 2455−2460.
(3) Wadia, C.; Alivisatos, A. P.; Kammen, D. M. *Environ. Sci. Technol.* **2009**, *43*, 2072−2077.
(4) Shin, B.; Gunawan, O.; Zhu, Y.; Bojarczuk, N. A.; Chey, S. J.; Guha, S. *Prog. Photovoltaics* **2011**, *21*, 72−76.
(5) Todorov, T. K.; Tang, J.; Bag, S.; Gunawan, O.; Gokmen, T.; Zhu, Y.; Mitzi, D. B. *Adv. Energy Mater.* **2012**, *3*, 34−38.
(6) Wang, K.; Gunawan, O.; Todorov, T.; Shin, B.; Chey, S. J.; Bojarczuk, N. A.; Mitzi, D.; Guha, S. *Appl. Phys. Lett.* **2010**, *97*, 143508−3.
(7) Katagiri, H.; Jimbo, K.; Yamada, S.; Kamimura, T.; Maw, W. S.; Fukano, T.; Ito, T.; Motohiro, T. *Appl. Phys. Express* **2008**, *1*, 041201−2.
(8) Scragg, J. J.; Berg, D. M.; Dale, P. J. *J. Electroanal. Chem.* **2010**, *646*, 52−59.
(9) Kumar, Y. B. K.; Babu, G. S.; Bhaskar, P. U.; Raja, V. S. *Sol. Energy Mater. Sol. Cells* **2009**, *93*, 1230−1237.
(10) Guo, Q. J.; Hillhouse, H. W.; Agrawal, R. *J. Am. Chem. Soc.* **2009**, *131*, 11672−11673.
(11) Todorov, T. K.; Reuter, K. B.; Mitzi, D. B. *Adv. Mater.* **2010**, *22*, E156−E159.
(12) Mitzi, D. B.; Gunawan, O.; Todorov, T. K.; Wang, K.; Guha, S. *Sol. Energy Mater. Sol. Cells* **2011**, *95*, 1421−1436.
(13) Steinhagen, C.; Panthani, M. G.; Akhavan, V.; Goodfellow, B.; Koo, B.; Korgel, B. A. *J. Am. Chem. Soc.* **2009**, *131*, 12554−12555.
(14) Riha, S. C.; Parkinson, B. A.; Prieto, A. L. *J. Am. Chem. Soc.* **2009**, *131*, 12054−12055.
(15) Choubrac, L.; Lafond, A.; Guillot-Deudon, C.; Moelo, Y.; Jobic, S. *Inorg. Chem.* **2012**, *51*, 3346−3348.
(16) Guo, Q.; Ford, G. M.; Yang, W. C.; Walker, B. C.; Stach, E. A.; Hillhouse, H. W.; Agrawal, R. *J. Am. Chem. Soc.* **2010**, *132*, 17384−17386.
(17) Chen, S. Y.; Gong, X. G.; Walsh, A.; Wei, S. H. *Appl. Phys. Lett.* **2009**, *94*, 041903−3.
(18) Paier, J.; Asahi, R.; Nagoya, A.; Kresse, G. *Phys. Rev. B* **2009**, *79*, 115126−8.
(19) Lu, X.; Zhuang, Z.; Peng, Q.; Li, Y. *Chem. Commun.* **2011**, *47*, 3141−3143.

(20) Singh, A.; Geaney, H.; Laffir, F.; Ryan, K. M. *J. Am. Chem. Soc.* **2012**, *134*, 2910−2913.
(21) Kang, C.-C.; Chen, H.-F.; Yu, T.-C.; Lin, T.-C. *Mater. Lett.* **2013**, *96*, 24−26.
(22) Zou, Y.; Su, X.; Jiang, J. *J. Am. Chem. Soc.* **2013**, *135*, 18377−18384.
(23) Chen, S.; Walsh, A.; Luo, Y.; Yang, J.-H.; Gong, X. G.; Wei, S.-H. *Phys. Rev. B* **2010**, *82*, 195203−8.
(24) Regulacio, M. D.; Ye, C.; Lim, S. H.; Bosman, M.; Ye, E.; Chen, S.; Xu, Q.-H.; Han, M.-Y. *Chem.—Eur. J.* **2012**, *18*, 3127−3131.
(25) Cattley, C. A.; Cheng, C.; Fairclough, S. M.; Droessler, L. M.; Young, N. P.; Warner, J. H.; Smith, J. M.; Assender, H. E.; Watt, A. A. R. *Chem. Commun.* **2013**, *49*, 3745−3747.
(26) Mainz, R.; Singh, A.; Levcenko, S.; Klaus, M.; Genzel, C.; Ryan, K. M.; Unold, T. *Nature Comm.* **2014**, *5*, 3133−10.
(27) Fernandes, P. A.; Salomé, P. M. P.; da Cunha, A. F. *J. Alloys Compd.* **2011**, *509*, 7600−7606.
(28) Sarswat, P. K.; Free, M. L.; Tiwari, A. *Phys. Status Solidi B* **2011**, *248*, 2170−2174.
(29) Cheng, A. J.; Manno, M.; Khare, A.; Leighton, C.; Campbell, S. A.; Aydil, E. S. *J. Vac. Sci. Technol., A* **2011**, *29*, 051203−11.
(30) Platzer-Björkman, C.; Scragg, J.; Flammersberger, H.; Kubart, T.; Edoff, M. *Sol. Energy Mater. Sol. Cells* **2012**, *98*, 110−117.
(31) Woo, K.; Kim, Y.; Moon, J. *Energy Environ. Sci.* **2012**, *5*, 5340−5345.
(32) Munce, C. G.; Parker, G. K.; Holt, S. A.; Hope, G. A. *Colloids Surf., A* **2007**, *295*, 152−158.
(33) Cheng, Y. C.; Jin, C. Q.; Gao, F.; Wu, X. L.; Zhong, W.; Li, S. H.; Chu, P. K. *J. Appl. Phys.* **2009**, *106*, 123505−5.
(34) Mehdi, A.; Mohamad, M. B. M.; Hosein, E. *Phys. Scr.* **2012**, *85*, 035603−3.
(35) Fan, F.-J.; Wu, L.; Gong, M.; Chen, S. Y.; Liu, G. Y.; Yao, H.-B.; Liang, H.-W.; Wang, Y.-X.; Yu, S.-H. *Sci. Rep.* **2012**, *2*, 952−6.
(36) Davis, R. E.; Nakshbendi, H. F. *J. Am. Chem. Soc.* **1962**, *84*, 2085−2090.
(37) Thomson, J. W.; Nagashima, K.; Macdonald, P. M.; Ozin, G. A. *J. Am. Chem. Soc.* **2011**, *133*, 5036−5041.
(38) Kubaschewski, O.; Alcock, C. B.; Spencer, P. J. *Materials Thermochemistry,* 6th ed.; Pergamon: New York, 1993.
(39) Walsh, A.; Chen, S.; Wei, S.-H.; Gong, X.-G. *Adv. Energy Mater.* **2012**, *2*, 400−409.
(40) Petrov, K. A.; Andreev, L. N. *Russ. Chem. Rev.* **1971**, *40*, 505−524.
(41) Katagiri, H. *Thin Solid Films* **2005**, *480−481*, 426−432.
(42) A. J. Bard, L. R. F. *Electrochemical Methods: Fundamentals and Applications;* Wiley: New York 1980, 1−864.
(43) Huang, S.; Zou Z, L. W. *J. Phys. D: Appl. Phys.* **2013**, *46*, 235108−6.
(44) Haight, R.; Barkhouse, A.; Gunawan, O.; Shin, B.; Copel, M.; Hopstaken, M.; Mitzi, D. B. *Appl. Phys. Lett.* **2011**, *98*, 253502−3.